ELSEVIER

Journal of Fluids and Structures 23 (2007) 1149–1167

JOURNAL OF FLUIDS AND STRUCTURES

www.elsevier.com/locate/jfs

Viscous waves and wave-structure interaction in a tank using adapting quadtree grids

D.M. Greaves*

Department of Architecture and Civil Engineering, University of Bath, Claverton Down BA2 7AY, UK

Received 2 June 2006; accepted 12 April 2007
Available online 13 June 2007

Abstract

Viscous waves and waves over a submerged cylinder in a stationary tank are simulated using a volume-of-fluid numerical scheme on adaptive hierarchical grids. A high resolution interface-capturing method is used to advect the free surface interface and the Navier–Stokes equations are discretised using finite volumes with collocated primitive variables and solved using a Pressure Implicit with Splitting of Operators (PISO) algorithm. The cylinder is modelled by using the technique of Cartesian cut cells. Results of flow of a single fluid past a cylinder at Reynolds number $Re = 100$ are presented and found to agree well with experimental and other numerical data. Viscous free surface waves in a tank are simulated using uniform and quadtree grids for Reynolds numbers in the range from 2 to 2000, and the results compared against analytical solutions where available. The quadtree-based results are of the same accuracy as those on the equivalent uniform grids, and retain a sharp interface at the free surface while leading to considerable savings in both storage and CPU requirements. The nonlinearity in the wave is investigated for a selection of initial wave amplitudes. A submerged cylinder is positioned in the tank and its influence on the waves as well as the hydrodynamic loading on the cylinder is investigated.

Keywords: Adaptive quadtree grids; Volume of fluid; Free surface; Fluid structure interaction; Cartesian cut cells; Hydrodynamic loading

1. Introduction

There are many engineering applications where simulation of a viscous fluid with a free surface is important. For example, wave sloshing in tanks, green water on ship decks, wave loading and run-up on marine and coastal structures. Fully nonlinear waves and wave-body interactions have been solved by potential-based methods (Dommermuth and Yue, 1987; Ma et al., 2001a, b) for inviscid fluid flow, and useful results obtained for inertia driven effects, such as diffraction and wave impact loading. However, in some situations, such as the response of a floating wave energy conversion device, flow separation, turbulence and wave breaking all make significant contributions to the fluid loading. In these cases, the fluid viscosity must be accounted for, which usually means solving the full Navier–Stokes equations or Reynolds Averaged Navier–Stokes (RANS) equations if the flow is turbulent. Accurate modelling of a viscous fluid free surface flow is an extremely challenging problem in CFD because of the moving air–water interface together with

*Tel.: +44 1225 383412; fax: +44 1225 386691.
E-mail address: d.m.greaves@bath.ac.uk

0889-9746/$ - see front matter © 2007 Elsevier Ltd. All rights reserved.
doi:10.1016/j.jfluidstructs.2007.04.004

the nonlinear governing equations and boundary conditions. To model wave breaking a two-fluid approach may be taken, in which the fluid flow equations are solved both in air and water so that complex free surface motions can be modelled. The accuracy of the simulation depends on calculating the correct position of the air/water interface throughout the wave motion, and this becomes especially difficult when the wave overturns and merges with the water surface or when the interface breaks up into spray.

Various techniques by which to predict the position of a moving free surface may be classified as interface tracking methods, which include moving mesh, front tracking [e.g. Hyman (1984)] and particle tracking schemes [e.g. Monaghan (1994)]; and interface-capturing methods, which include volume of fluid (VoF) and level set techniques (Losasso et al., 2005). Moving mesh and front tracking methods may be accurate, but can only calculate waves up to the limit of breaking as the free surface has to be single valued. Particle tracking methods tend to be expensive, although so-called meshless methods, such as smooth particle hydrodynamics, SPH, described by Monaghan (1994) and the Meshless Local Petrov–Galerkin (MLPG) method described by Lin and Atluri (2001) have become more popular recently. These have the advantage of eliminating the need for complicated mesh boundary tracking, as they rely on integrations over a distribution of points rather than a closed mesh. On the other hand, front capturing methods can be used for modelling large-scale deformations of the interface, including wave break-up and merging. Front capturing methods differ from front tracking in that the solution is calculated in the combined air and water fluid domains, with the fluid properties changing at the interface. The interface is then located from the zero contour of a distance function in the case of level set [see Causon (1996)] or from the volume fraction field in the VoF method introduced by Hirt and Nichols (1981).

The basic VoF methodology is robust and flexible and VoF schemes are widely used [e.g. Hirt and Nichols (1981), Tomiyama et al. (1993), Andrillon and Alessandrini (2004)]. The major drawbacks of this method are its tendency to smear the interface and the high CPU cost due to the need for fine grids and small time steps. In order to overcome these problems, a new method is proposed in this work in which the high resolution Compressive Interface Capturing Scheme for Arbitrary Meshes (CICSAM) interface advection scheme, derived by Ubbink (1997), is implemented on adapting quadtree grids, described by Greaves and Borthwick (1998). The Navier–Stokes equations are solved using a version of Issa's (1986) PISO together with collocated variables. Special interpolations are needed at the interface between panels of different size, i.e. at hanging nodes. Adapting quadtree grids provide extra resolution locally in areas of interest and have proved successful in the simulation of separated flows by Greaves and Borthwick (1998), where the overall size of the grid is reduced significantly for a given accuracy by providing high resolution where the flow variables are changing most rapidly. The adapting quadtree grids are combined with Cartesian cut cells [see Qian et al. (2003)] in order to model the curved cylinder boundary smoothly.

The work described here builds on earlier work in which a quadtree VoF method was developed for two-fluid interface flows and applied to simulation of water column collapse involving large-scale deformation of the free surface described by Greaves (2004, 2005). Here, the scheme is applied to a series of standing waves in a tank for which the linearised analytical solution is available. A major contribution of the present work is the incorporation of Cartesian cut cells with the adaptive quadtree grid-based VoF method. This enables a curved body, such as the cylinder, to be modelled smoothly and hence wide range of fluid–structure interaction applications to be tackled. Moving boundaries are easily accommodated by the Cartesian cut cell method, simply by recalculating the cuts between the boundary contour and background grid for as long as the motion continues.

The paper is organised as follows. First, the mathematical formulation and discretisation procedure is discussed in Section 2; then, quadtree grids are described in Section 3, and in Section 4 implementation of the Cartesian cut cell technique on quadtree grids is described. Results are presented in Section 5; initially vortex shedding flow past a cylinder in a single fluid at $\mathrm{Re} = 100$ is simulated to demonstrate the quadtree grid adaptation with Cartesian cut cells. Next, the adapting quadtree grids, combined with CICSAM interface advection, are used to calculate viscous waves in a stationary tank, with the grid adaptation following the movement of the free surface. Finally, the influence of a submerged cylinder on the viscous waves in a tank is investigated by combining the free surface method with Cartesian cut cells for the cylinder. Conclusions and recommendations for further work are given in Section 6.

2. Mathematical formulation

The governing equations in primitive form for a two-dimensional incompressible flow are the mass conservation equation

$$\frac{\partial(\rho u)}{\partial x} + \frac{\partial(\rho v)}{\partial y} = 0 \tag{1}$$

and the Navier–Stokes momentum conservation equations

$$\frac{\partial u}{\partial t}+\frac{\partial u^2}{\partial x}+\frac{\partial uv}{\partial y}=-\frac{1}{\rho}\frac{\partial p}{\partial x}+\nu\nabla^2 u, \tag{2}$$

$$\frac{\partial v}{\partial t}+\frac{\partial uv}{\partial x}+\frac{\partial v^2}{\partial y}=-g-\frac{1}{\rho}\frac{\partial p}{\partial y}+\nu\nabla^2 v, \tag{3}$$

where x and y define an orthogonal Cartesian coordinate system, u and v are the corresponding velocity components, t is time, p is pressure, ρ is the fluid density, g is the gravitational acceleration and ν is the fluid kinematic viscosity.

For situations where the fluid viscosity is variable, such as the two-fluid flow simulations considered here, an extra diffusion term appears in the momentum equations which, written in tensor form, is given by

$$\frac{\partial}{\partial x_j}\left(\nu\frac{\partial u_j}{\partial x_j}\right). \tag{4}$$

Thus, the expanded momentum equations become

$$\frac{\partial u}{\partial t}+\frac{\partial u^2}{\partial x}+\frac{\partial uv}{\partial y}=-\frac{1}{\rho}\frac{\partial p}{\partial x}+\nu\nabla^2 u+\frac{\partial}{\partial x}\left(\nu\frac{\partial u}{\partial x}\right)+\frac{\partial}{\partial y}\left(\nu\frac{\partial v}{\partial x}\right), \tag{5}$$

$$\frac{\partial v}{\partial t}+\frac{\partial uv}{\partial x}+\frac{\partial v^2}{\partial y}=-g-\frac{1}{\rho}\frac{\partial p}{\partial y}+\nu\nabla^2 v+\frac{\partial}{\partial x}\left(\nu\frac{\partial u}{\partial y}\right)+\frac{\partial}{\partial y}\left(\nu\frac{\partial v}{\partial y}\right). \tag{6}$$

The governing equations are discretised using finite volumes with collocated primitive variables. In order to solve for the velocity and pressure field, we need to couple the momentum and continuity equations in some way. Various approaches to this are used in the literature. In this work, Issa's (1986) PISO algorithm is used, which stands for Pressure Implicit with Splitting of Operators, in which the momentum equation is substituted into the continuity equation to derive a Poisson equation for pressure. Adams-Bashworth time stepping [see Ferziger and Perić (1996)] is used for the time dependent calculations.

The PISO algorithm is combined with a VoF scheme for the two-fluid flow simulations. When considering the incompressible flow of two immiscible fluids, the divergence free velocity field $\mathbf{u}(x,t)$ obeys

$$\boldsymbol{\nabla}\cdot\mathbf{u}=0. \tag{7}$$

The location of the two fluids is specified using a volume fraction function, C, with $C=1$ inside one fluid and $C=0$ in the other. Cells for which C lies between 0 and 1 contain the interface. The volume conservation of the first fluid can be expressed as

$$\frac{\partial C}{\partial t}+\boldsymbol{\nabla}\cdot(\mathbf{u}C)=0. \tag{8}$$

A common tendency of the VoF method is that the interface may be smeared over many cells. Much research effort has been spent recently (Ubbink and Issa, 1999; Qian et al., 2003; Kleefsman and Veldman, 2004) to develop new techniques for solving the volume fraction equation in a way that keeps the interface sharp.

The original VoF method of Hirt and Nichols (1981) has a fluxing scheme that uses either upwinding or a downwinding donor–acceptor cell approach depending on the local orientation of the interface. The advantage of the upwind scheme is that it is stable, but it is diffusive and may spread the interface over many cells. The downwind scheme is unstable, but sharpens the interface and so is advantageous in interface tracking. Various VoF fluxing methods have been developed, most of which aim for a balance between the stability advantages of the upwind scheme and the front sharpening advantages of the downwind scheme.

Here, we use Ubbink's (1997) compressive differencing scheme for discretisation of the volume fraction equation named CICSAM. In the CICSAM scheme, the cell face values of C, used in the discretised volume fraction equation, are determined from a combination of the Convection Boundedness Criteria (CBC) value and the Ultimate Quickest (UQ) value. The weighting factor used to combine the CBC and UQ contributions takes into account the orientation of the interface and the direction of motion. This scheme is described in detail by Greaves (2004) and used for simulation of water column collapse and subsequent interaction with an obstacle by Greaves (2005).

3. Quadtree grids

Quadtree grid generation, grid reference numbering schemes, grid data retrieval and neighbour finding routines are described in detail in previous publications [e.g. Greaves and Borthwick (1998), Yiu et al. (1995)] and so are not discussed here. Similarly, the treatment of hanging nodes and the interpolation and extrapolation necessary during quadtree grid adaptation are described by Greaves (2004, 2005). Quadtree grids can be readily adapted by the addition and removal of panels throughout a time dependent simulation. For the wave simulations, grid refinement is used to follow the movement of the interface and for the separated flow case, grids are refined in areas of high flow vorticity.

Remeshing of the grid operates by dividing a cell into four if it lies within a specified distance from the interface or for separated flow cases has a vorticity value greater than a specified maximum. Derefinement takes place by removing four sibling cells and replacing them with their parent if each of the four sibling cells lies away from the interface band or, for separated flow cases, if each has vorticity less than a specified minimum. Velocity and pressure variables are interpolated onto new cells using bi-linear interpolation from the neighbours of the divided cell. Alternatively, when four sibling cells are removed and replaced with their parent, the variables assigned to the parent are the average of the four sibling values. For the wave simulations, the grid is adapted at the edge of the interface band, which lies wholly within either the air or water phase, and so the volume fraction for each of the removed siblings and their parent will be either 0 or 1. The technique has been demonstrated for extreme free surface motions, including wave break-up and spray by Greaves (2005).

4. Cartesian cut cells

Due to their Cartesian nature, smooth curves modelled by the quadtree grids will have a stepped approximation. This is illustrated in Fig. 1, where a circular cylinder is located in the grid; it is clear that no matter how refined the quadtree is at the cylinder, the smooth boundary will inevitably have a staircase approximation. This modelling error can be eliminated by using the Cartesian cut cell technique, in which the smooth shape of the body is cut out of the grid, leaving cut cells around the body boundary, as in Fig. 2. The quadtree grid is generated by recursive subdivision about seeding points that lie around the surface of the cylinder. Cells within the quadtree grid are then searched to identify those containing seeding points. A given boundary cell may contain more than one seeding point, and the search continues until the first and last seeding point in each cell has been identified. The seeding points can then be used to define the cut face and to assign a type to each cut cell. The type assignment depends on the orientation of the cut face and is described by Yang et al. (1997). Once this has been assigned, parameters of the cut cell such as fluid volume, centroid coordinates (at which variables are stored) and cell face coordinates may be readily determined.

The cut cell process usually generates some very small cut cells around the boundary and these may require very small time steps for stability. Small cut cells can be seen around the cylinder in Fig. 2, which is also shown enlarged in Fig. 3. The problem of very small cut cells may be overcome by merging cut cells that have fluid volume less than a specified minimum. If the specified minimum is 0.5 of the finest quadtree cell, merging produces the grid shown in Fig. 4 and may result in some of the merged cells being larger than the finest quadtree cell. Tseng and Ferziger (2003) suggest an alternative to merging, known as the Ghost-cell Immersed Boundary Method (GCIBM). In this method, the velocity and pressure fields are extrapolated from neighbouring fluid cells to ghost cells, lying out of the fluid domain, in order to enforce boundary conditions at the boundary. However, we have not implemented this approach here.

Special interpolations are used to calculate gradients and variables at faces for the finite volume scheme at these cut cells. Following recommendations made by Qian et al. (2005) gradients for cut cells are calculated in two stages. First, the fluid and solid gradients on the cut cells are calculated from neighbouring cell values with a slope limiter function applied to prevent over- or under-shoots and to maintain a sharp interface. This is illustrated for the cut cell P shown in Fig. 5.

Variables are interpolated to the fictional mirror node R. If no-slip wall boundary conditions are used, the pressure and velocity are

$$p_R = p_P - \rho_P g\left(n_y|RP|\right), \tag{9}$$

$$\mathbf{u}_R = \mathbf{u}_P - 2(\mathbf{u}_P \cdot \mathbf{n})\mathbf{n}, \tag{10}$$

where ρ_P is the density at cell P, g is the acceleration due to gravity for wave cases, $|RP|$ is the distance between nodes R and P, $\mathbf{n}$ is the unit normal vector to the cut face and n_x and n_y are the unit vectors along x- and y-directions, respectively. The fluid, superscript f, and solid, superscript s, gradients are calculated separately in each

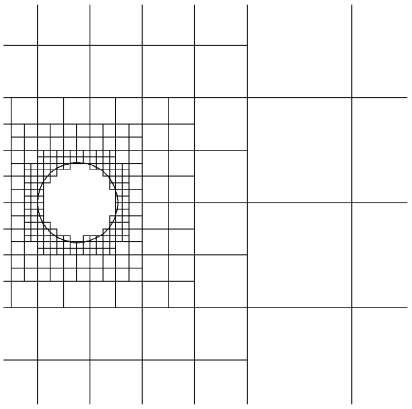

Fig. 1. Quadtree grid for a cylinder.

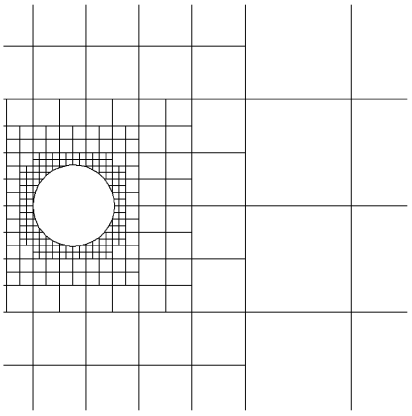

Fig. 2. Quadtree cut cell grid for a cylinder.

coordinate direction:

$$\Phi_x^f = G\left(\frac{\Phi_E - \Phi_P}{x_E - x_P}, \frac{\Phi_P - \Phi_W}{x_P - x_W}\right) \quad \text{and} \quad \Phi_y^f = G\left(\frac{\Phi_N - \Phi_P}{y_N - y_P}, \frac{\Phi_P - \Phi_S}{y_P - y_S}\right), \tag{11,12}$$

$$\Phi_x^s = G\left(\frac{\Phi_R - \Phi_P}{x_R - x_P}, \frac{\Phi_P - \Phi_W}{x_P - x_W}\right) \quad \text{and} \quad \Phi_y^s = G\left(\frac{\Phi_R - \Phi_P}{y_R - y_P}, \frac{\Phi_P - \Phi_S}{y_P - y_S}\right), \tag{13,14}$$

where G is a slope limiter function and Φ represents a general variable and may be velocity or pressure. Here, the van Leer limiter is used,

$$G(a,b) = \frac{a|b| + |a|b}{|a| + |b|}. \tag{15}$$

Qian et al. (2005) also suggest other gradient limiters such as the k-limiter, which corresponds to the superbee or minmod limiter depending on the value of k, and the hyperbee limiter.

Next, a length average technique involving the aperture length open to fluid and solid for a given cut cell is used to convert the fluid and solid gradients to a unique gradient for each direction in each cut cell,

$$\Phi_x = \frac{\Delta y_s \Phi_x^s + \Delta y_f \Phi_x^f}{\Delta y}, \quad \Phi_y = \frac{\Delta x_s \Phi_y^s + \Delta x_f \Phi_y^f}{\Delta x}, \tag{16,17}$$

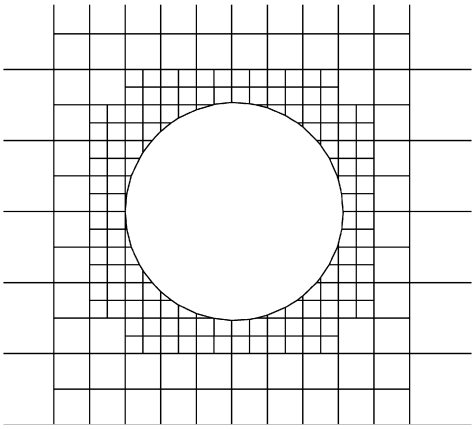

Fig. 3. Close-up of cut cells at the cylinder.

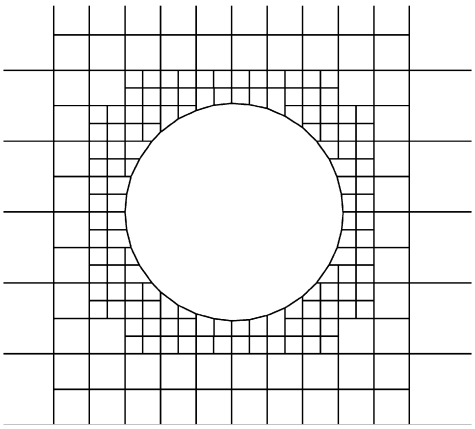

Fig. 4. Merged cut cells.

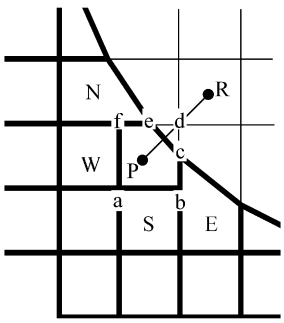

Fig. 5. Calculation of gradients at a cut cell.

where Δy_s is the distance |cd| in Fig. 5, Δy_f is |bc|, Δx_s is |de|, Δx_f is |fe| and Δx and Δy are the uncut cell side lengths |ab| and |af|. Finally, the overall cell gradient is a combination of the gradients in x- and y-directions

$$\nabla \boldsymbol{\Phi}_P = \boldsymbol{\Phi}_x n_x + \boldsymbol{\Phi}_y n_y. \tag{18}$$

The value of a given variable may be determined at any position in the cut cell using

$$\boldsymbol{\Phi}(x,y) = \boldsymbol{\Phi}_P + \nabla\Phi_P \cdot \mathbf{r}, \tag{19}$$

in which $\mathbf{r}$ is the position vector from the cell centre to any position (x, y) within cell P. The face velocities at the centre of each face for a cut cell are calculated in this way in order to determine convective fluxes and to calculate pressure gradients in the momentum equations.

5. Results

5.1. Separated flow past a cylinder

The adaptive quadtree cut cell method is first tested for fluid flow past a cylinder at Reynolds number, $\mathrm{Re} = \rho u_{\mathrm{in}} d/\mu = 100$. Here, d is the cylinder diameter and u_{in} is the inlet velocity. The cylinder centre is positioned at $11.20d$ from the inlet, $31.54d$ from the right-hand boundary and $21.37d$ from top and bottom boundaries (see Fig. 6). No slip boundary conditions are used on the cylinder, free boundary conditions are applied on the right-hand, top and bottom walls and a steady unidirectional inlet velocity, $u = u_{\mathrm{in}}$, $v = 0$ is applied on the left-hand wall. The grid is initially refined around the cylinder boundary only, and as the vortex shedding flow develops, it adapts to areas of high vorticity. The quadtree grid has maximum division level of 10 at the cylinder and in the adapted region as it develops and a minimum background division level of 5. It is adapted every 20 time steps throughout the simulation and the non-dimensional time step size, $\Delta\tau = \Delta t d/u_{\mathrm{in}} = 0.001$. Fig. 6 shows the adapted quadtree grid, Fig. 7 shows the velocity vectors close to the cylinder and Fig. 8 the streamlines once vortex shedding has established at non-dimensional time, $\tau = 129$. Fig. 9 shows the time history of lift and drag force coefficients, calculated by integrating the pressure and viscous forces around the cylinder surface. The Strouhal number, $\mathrm{St} = f_s d/u_{\mathrm{in}}$ (where f_s is the vortex shedding frequency), is predicted to be $\mathrm{St} = 0.143$, the mean drag coefficient to be $c_{D\mathrm{ave}} = 1.36$ and the rms lift coefficient to be $c_{L\mathrm{rms}} = 0.209$, which agree reasonably well with experimental and numerical data given by Zhou and Graham (2000) who recorded values of $\mathrm{St} = 0.152$–0.174, $c_{D\mathrm{ave}} = 1.29$–1.82 and $c_{L\mathrm{rms}} = 0.14$–0.34. The hydrodynamic forces are nondimensionalised using

$$c_D = \frac{D}{\frac{1}{2}\rho(u_{\mathrm{in}})^2} \quad \text{and} \quad c_L = \frac{L}{\frac{1}{2}\rho(u_{\mathrm{in}})^2}. \tag{20}$$

5.2. Viscous waves in a container

5.2.1. Re = 200

A linearised analytical solution for small amplitude viscous waves in a rectangular tank has been derived by Wu et al. (2001) and is used to validate the new scheme for simulating viscous free surface waves. Wang et al. (2004) calculated

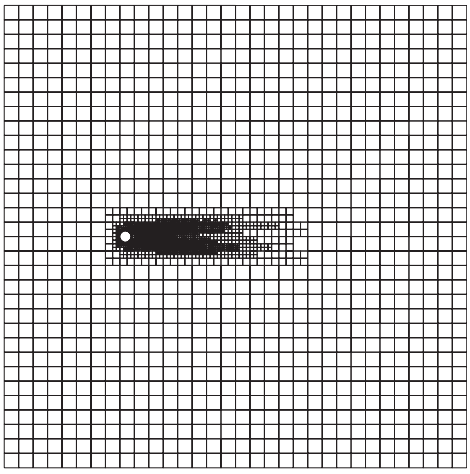

Fig. 6. $\tau = 129$ adapted quadtree grid.

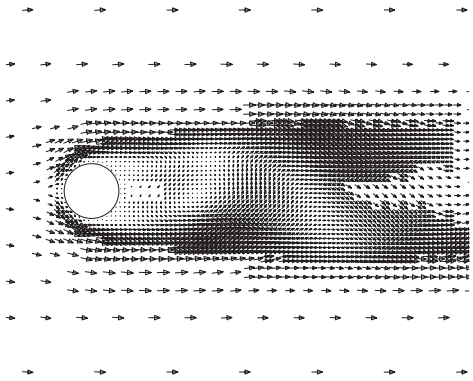

Fig. 7. $\tau = 129$ velocity vectors.

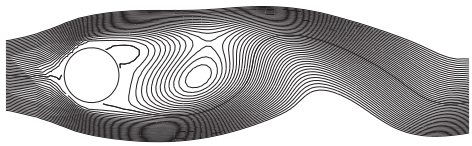

Fig. 8. $\tau = 129$ streamlines.

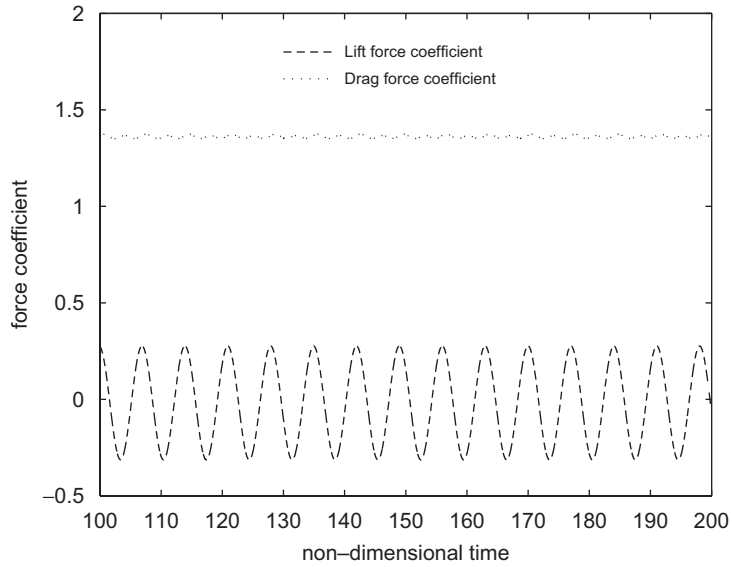

Fig. 9. Time history of c_D and c_L for $\mathrm{Re} = 100$.

similar viscous wave cases numerically. The length of the tank, $b = 2h$, where h is the mean water depth. The wave has initial surface elevation profile, $\eta = a\cos(2\pi x/b)$, where x is measured along the length of the tank and $a = 0.02h$ is the wave amplitude (see Fig. 10). The Reynolds number is calculated from $\mathrm{Re} = h\sqrt{gh}/v$, in which v is the kinematic viscosity. Initial conditions for velocity are zero, the pressure is set to hydrostatic and no-shear boundary conditions are applied on walls [following Wu et al. (2001)]. Initially, $\mathrm{Re} = 200$ waves are simulated using a series of adapting quadtree grids with refinement in a band surrounding the free surface and with nondimensional time step $\mathrm{d}\tau = \mathrm{d}t\sqrt{g/h} = 0.00044$. The time step used for these calculations was arrived at by trial and error. The reconstructed

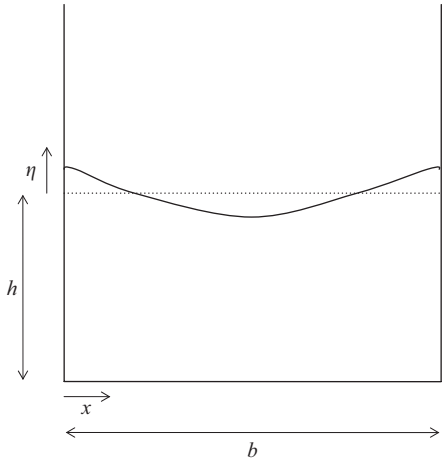

Fig. 10. Layout sketch for wave simulations.

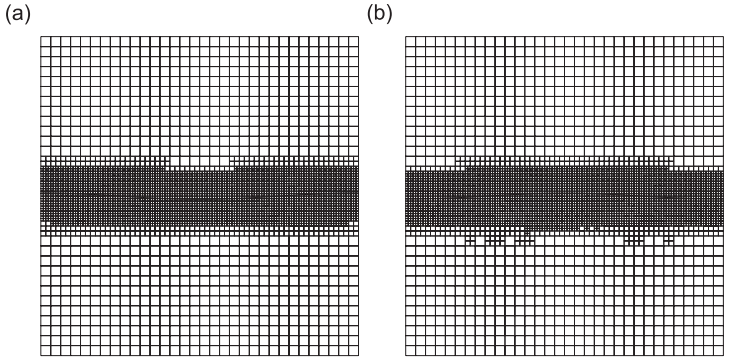

Fig. 11. Free surface and adapted quadtree grid: (a) $\tau = 0$, (b) $\tau = 1.754$.

free surface and adapted quadtree grid are plotted in Fig. 11(a) at nondimensional time, $\tau = 0$ and (b) at the first peak, $\tau = 1.754$. In this case, the maximum division level is 7 and the minimum division level (background grid resolution) is 5 and it will be referred to here as a 7×5 quadtree grid. The band around the interface is 10 cells wide. The number of cells in the interface band is arrived at by selecting the smallest band that will produce wave elevation history results to the same accuracy as a uniform grid of the maximum division level.

In Fig. 12, results of calculations of the $\mathrm{Re} = 200$ viscous wave in a tank using quadtree grids of different resolution, 6×4, 7×5 and 8×6 are plotted together with those calculated on a 128×128 square grid which has cells uniformly the same size as the smallest in the 7×5 quadtree grid. The wave elevation is nondimensionalised by the initial wave amplitude, $\eta = y/a$. The figure shows the wave elevation history recorded at the centre of the tank and the results all agree well with differences being discernable only at later times in the simulation. Results calculated on the 7×5 quadtree and equivalent uniform grid are identical, confirming that there is no loss of accuracy through the use of adapting quadtrees. Fig. 13 shows wave elevation histories calculated using four different time steps on the 7×5 quadtree grid, which converge to the smallest time step solution. The results in Figs. 12 and 13 together demonstrate spatial and temporal grid convergence of the method.

In Table 1, typical grid size and CPU per time step are given for a series of quadtree and equivalent uniform grids. All calculations were made on a SUNFIRE 480R with 16 Gb RAM, 4×900 MHz UltraSPARC-III+ CPUs, 2×36 Gb (internal) HDs running Solaris 8. It is shown earlier that through using adapting quadtree grids refined at the interface the same accuracy is achieved as with a grid refined uniformly throughout the domain. Furthermore, use of adapting quadtree grids leads to significant savings in both grid size and CPU; the 7×5 quadtree grid contains approximately 4.0 times less cells and requires approximately 4.2 times less CPU than the equivalent uniform grid.

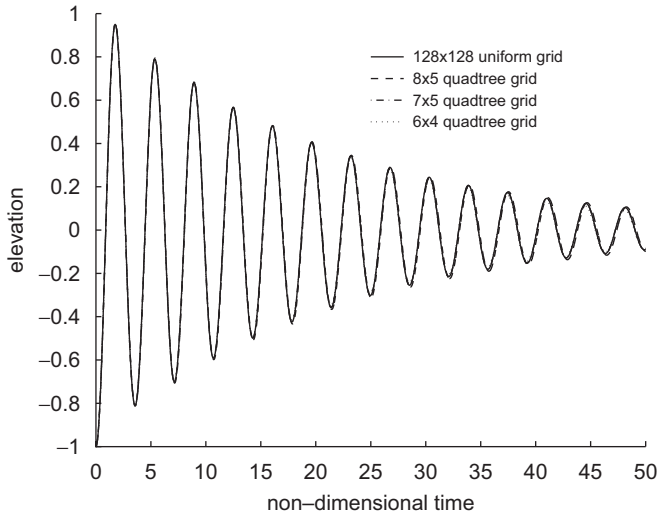

Fig. 12. Wave elevation history at the centre of the tank: comparison of quadtree grid sizes.

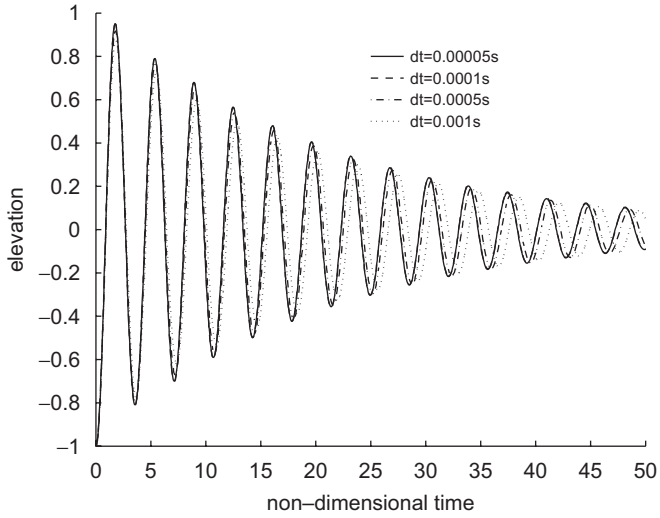

Fig. 13. Wave elevation history at the centre of the tank: comparison of time step.

Table 1
Summary of grid size and CPU data averaged over ten time steps

Grid type	Max level	Min level	Typical no. of cells	CPU per time step (s)
Uniform	5	5	1024	0.200
Quadtree	5	3	304	0.062
Uniform	6	6	4096	1.348
Quadtree	6	4	1048	0.436
Uniform	7	7	16384	9.465
Quadtree	7	5	4057	2.225

5.2.2. Re = 2, 20, 200 and 2000

In Figs. 14–17, time history results are plotted for waves in fluid of different viscosity, Re = 2, 20, 200 and 2000, together with the analytical solution published by Wu et al. (2001). In each case, the wave period is generally predicted well by the numerical scheme, but the wave amplitude is greater than the linearised analytical solution. One would expect the numerical solution to approach the linearised analytical solution more closely as the amplitude is reduced and to deviate further from it at larger amplitudes; this effect is observed to some extent in Section 5.2.3, but does not explain the large difference in amplitude in Figs. 14–17. The numerical prediction is closer to the linearised analytical solution for larger Reynolds number cases in which the fluid is less viscous. The convection terms are eliminated from the Navier–Stokes equations in the linearised analytical solution. Thus, the greater deviation from the analytical solution for the lower Reynolds number cases suggests that the convective terms have a stronger influence on the fluid motion than in the less viscous, higher Reynolds number fluid.

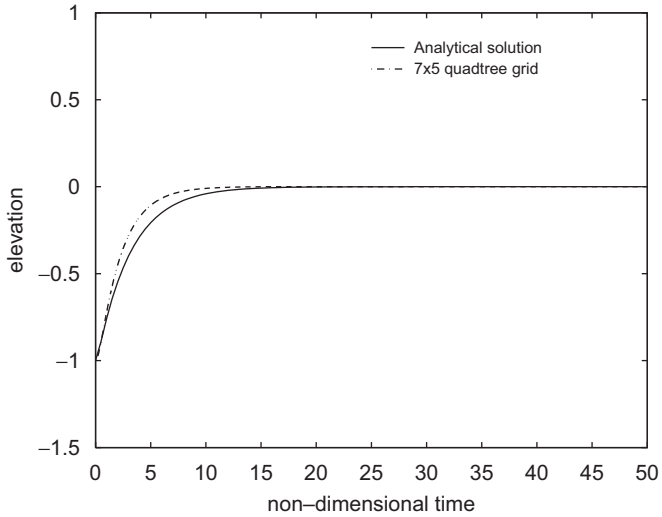

Fig. 14. Wave elevation history at the centre of the tank: Re = 2.

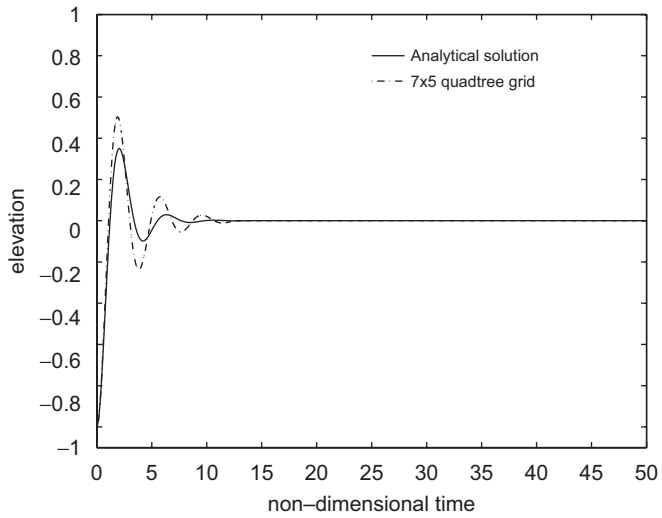

Fig. 15. Wave elevation history at the centre of the tank: Re = 20.

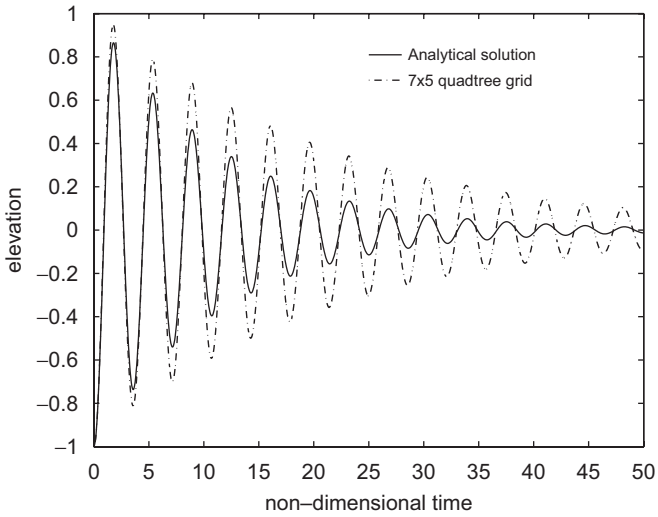

Fig. 16. Wave elevation history at the centre of the tank: Re = 200.

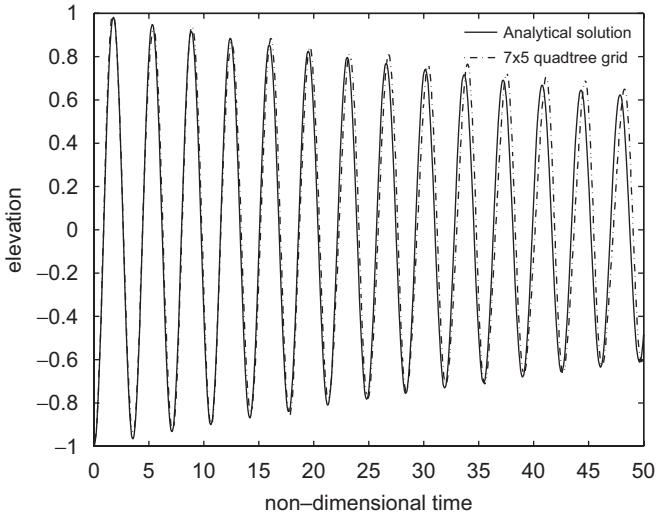

Fig. 17. Wave elevation history at the centre of the tank: Re = 2000.

5.2.3. Investigation of wave nonlinearity

Calculations are next made for waves with Re = 200 and a range of initial amplitudes, $a = 0.2h$, $0.06h$, $0.04h$, $0.02h$, $0.01h$, in order to investigate the effect of nonlinearity and to test the method for large amplitude motions. Results are summarised in Fig. 18. The four smaller amplitude cases all have similar time history behaviour, with differences evident in the size of peaks and troughs for the first few oscillations only. The largest amplitude case, $a = 0.2h$, however, exhibits clear nonlinear asymmetry as the peaks are significantly sharper than the troughs. This is confirmed when the wave profiles at the first five peaks and troughs are plotted together in Figs. 19 and 20 for linear and nonlinear waves. In Fig. 19, the linear small amplitude wave, $a = 0.02h$, can be compared with the nonlinear large amplitude wave, $a = 0.2h$, in Fig. 20. The velocity field and wave profile at the first peak and trough for the large amplitude wave are plotted in Figs. 21 and 22. These show how the quadtree grid has adapted to follow the large motions of the free surface, whilst maintaining a band of 10 cells around the interface.

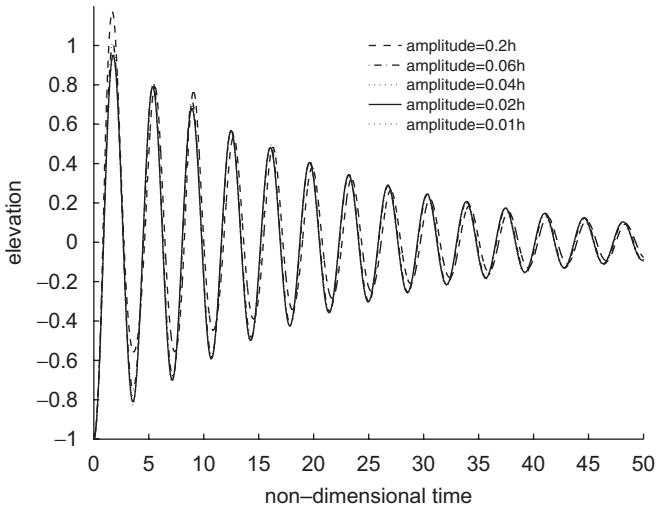

Fig. 18. Wave elevation history at the centre of the tank for Re = 200 wave with initial amplitudes, $a = 0.2h$, $0.06h$, $0.04h$, $0.02h$, $0.01h$.

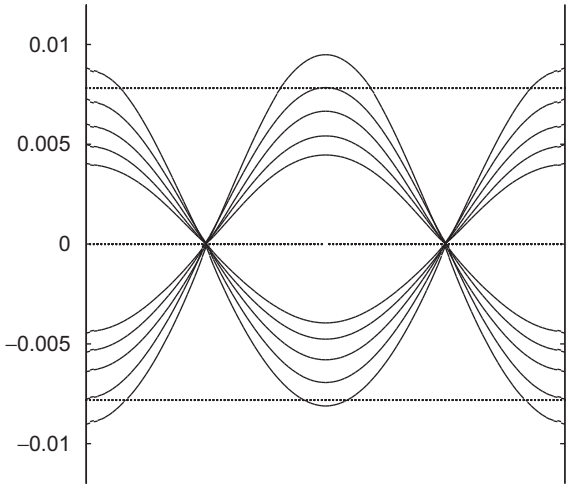

Fig. 19. First five peaks and troughs for $a = 0.02h$.

5.2.4. Waves in viscous fluid over a submerged cylinder

Preliminary results for viscous wave interactions with a submerged cylinder in the tank are presented here. A submerged cylinder of diameter $d = 0.2h$ (where h is the undisturbed depth of water in the tank) is positioned at the horizontal centre of the unit square tank at depth $0.5h$ below the mean water level. The fluid Reynolds number for the wave, $\mathrm{Re} = h\sqrt{gh}/\nu = 200$ and the initial wave amplitude $a = 0.02h$. A refinement band of 10 cells is maintained around the cylinder boundary as well as the interface and the 7×5 quadtree grid adapts dynamically at each time step. It would be possible to use different levels of refinement at the cylinder and free surface if necessary, but a maximum division level of 7 at both locations is used here. The calculation takes 3.11 s CPU per timestep using the SUNFIRE 480R mentioned above. The initial and adapted grids at the first peak are shown in Fig. 23 and the time history of the wave recorded at the centre of the tank is plotted in Fig. 24 together with the wave-only case without a cylinder for comparison. The results show that the presence of the submerged cylinder in the tank acts to damp out the wave motion at the free surface. A slight time lag in the wave history is also evident in the cylinder case when compared with the wave-only case in Fig. 24.

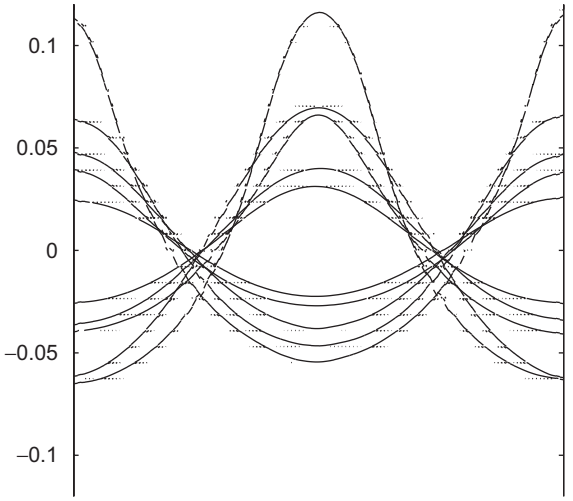

Fig. 20. First five peaks and troughs for $a = 0.2h$.

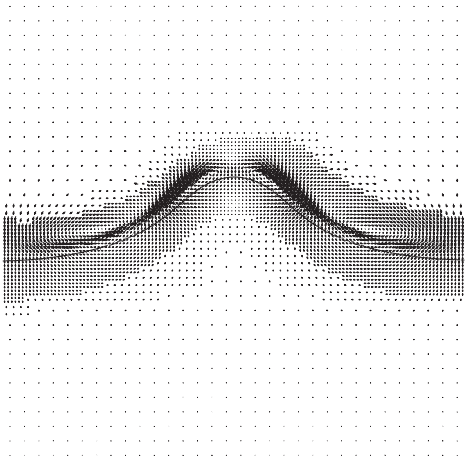

Fig. 21. First peak and velocity field, $a = 0.2h$.

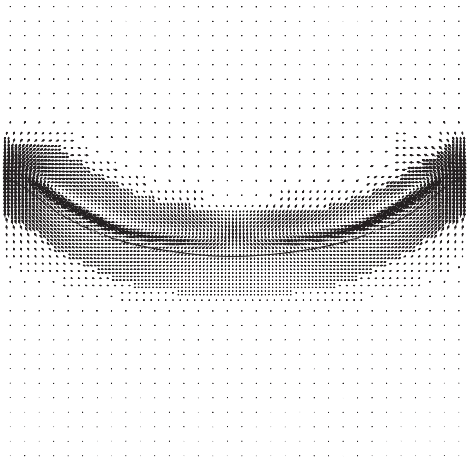

Fig. 22. First trough and velocity field, $a = 0.2h$.

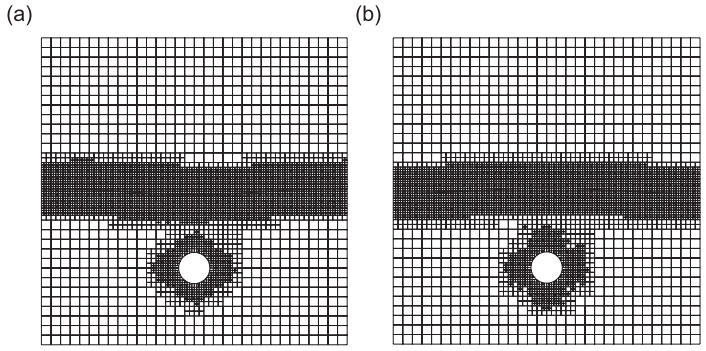

Fig. 23. Free surface and adapted quadtree grid: (a) $\tau = 0$, (b) $\tau = 1.754$.

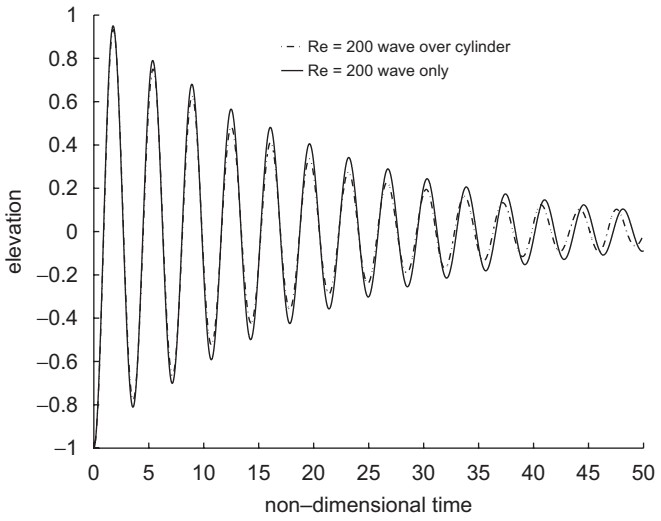

Fig. 24. Wave elevation time history at the centre of the tank, Re = 200.

The force on the cylinder is calculated by integrating the pressure and viscous shear stress around the cylinder and recorded at each time step. The force can be nondimensionalised in the following way:

$$c_F = \frac{F}{\frac{1}{2}\rho U_m^2}, \tag{21}$$

where U_m is the maximum velocity at the cylinder position when no cylinder is present. The force can be considered comprising a component in phase with the velocity, U, the drag force, and a component in phase with the fluid acceleration, $\mathrm{d}U/\mathrm{d}t$, the inertia force, and expressed using Morison's equation,

$$F = \frac{1}{2}\rho U|U| d c_D + \frac{1}{4}\pi\rho d^2 \frac{\mathrm{d}U}{\mathrm{d}t} c_M. \tag{22}$$

Morison's equation depends on experimental determination of the drag and inertia force coefficients, c_D and c_M. Bearman et al. (1985) measured forces on cylinders in experiments using a U-tube to generate harmonically varying fluid velocity and acceleration in-line with the cylinder. This restricts the fluid motion to a single component, so that Morison's equation can be applied and the drag and inertia components extracted from the measured force time history by Fourier averaging.

A dominant force in the wave cases considered here is due to hydrostatic pressure, which can be eliminated by subtracting the instantaneous hydrostatic components at each time step. What remains in the force is due entirely to the

hydrodynamic effects under the wave. After removing the hydrostatic part, a Morison equation type analysis such as given by Bearman et al. (1985) could be performed; however, the force coefficients cannot be compared directly as the flow kinematics under a wave are more complicated than purely in-line velocities occurring in U-tube experiments. Sarpkaya (1981) suggests that Fourier averaging may still be used for deriving c_D and c_M in regular waves, but is not suitable for the cases calculated here, in which the wave is strongly damped by the fluid viscosity (Figs. 24 and 26). The horizontal and vertical force coefficients (with the hydrostatic part subtracted) are plotted in Fig. 25.

Results are also calculated for a submerged cylinder under the Re = 20 wave. Fig. 26 shows the wave history for this case plotted together with the wave only solution and in Fig. 27, the time history of horizontal and vertical force coefficients on the cylinder are plotted. The wave is damped by the presence of the submerged cylinder as found for the Re = 200 case above.

For each wave Reynolds number investigated, the horizontal force is approximately zero, the vertical force is much larger and oscillates with the same frequency as the wave motion. If we consider the fluid kinematics under the centre of the symmetric cosine wave, the velocity is mainly in the vertical direction and this explains why the horizontal

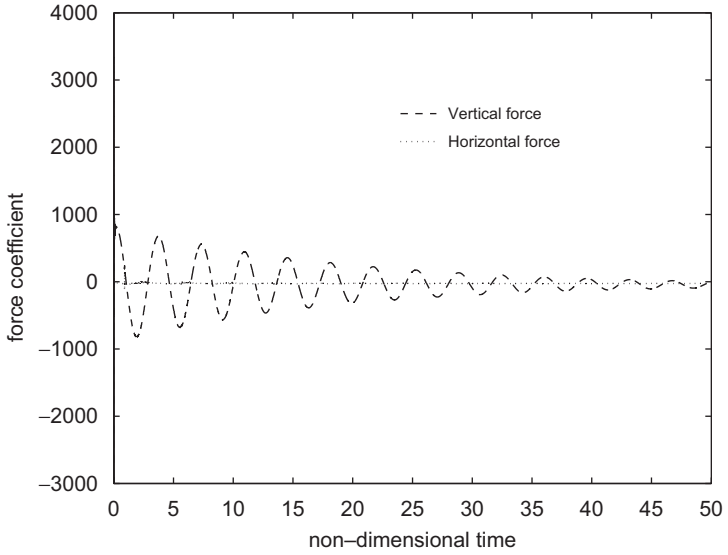

Fig. 25. Time history of forces on submerged cylinder, Re = 200.

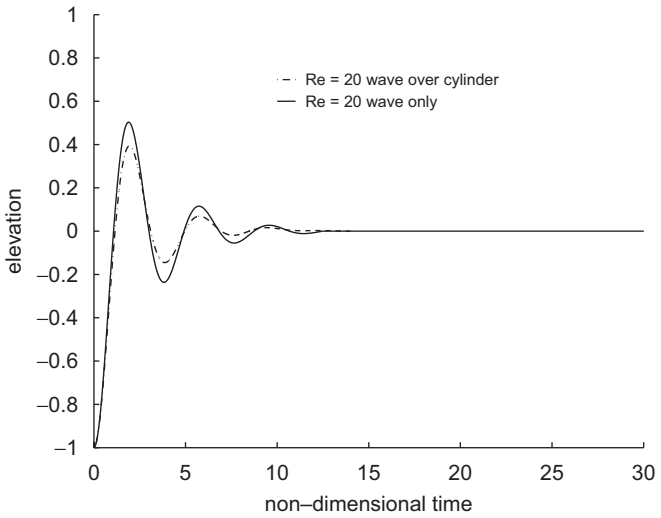

Fig. 26. Wave elevation history at the centre of the tank, Re = 20.

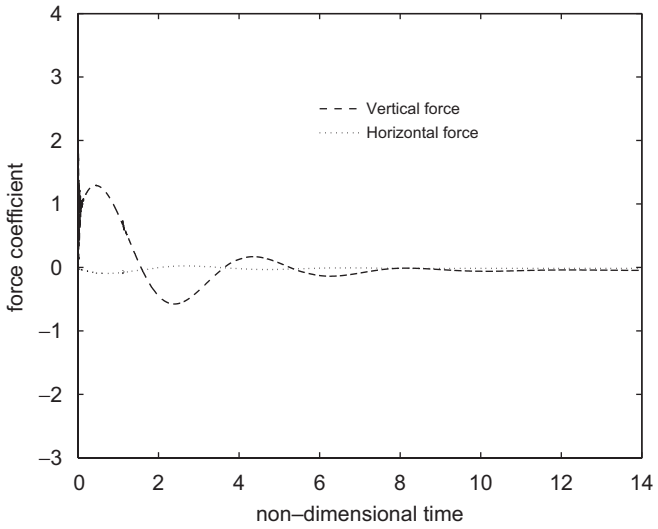

Fig. 27. Time history of forces on submerged cylinder, Re = 20.

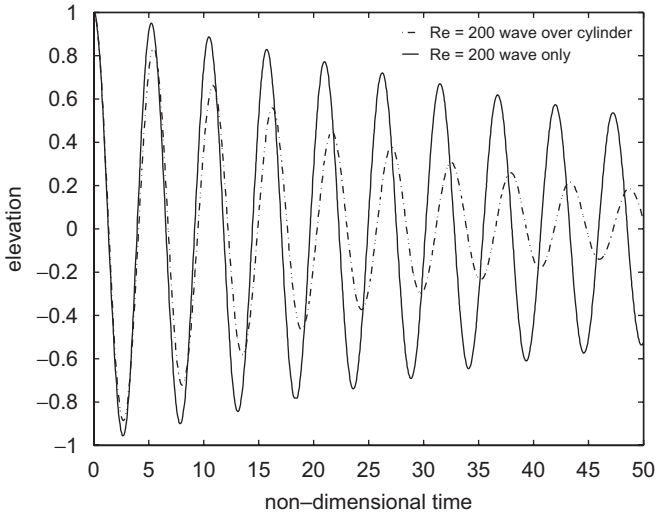

Fig. 28. Wave elevation history at the left-hand wall, Re = 200.

hydrodynamic force is insignificant compared with the vertical hydrodynamic force. However, the vertical hydrodynamic force is exactly 180° out of phase with the wave motion and can be seen from Fig. 25 to be a maximum when the wave trough is over the cylinder and the force is at its minimum when the wave crest is over the cylinder. This suggests that the vertical hydrodynamic force is dominated by inertia and follows the vertical fluid acceleration under the wave. For cases, such as this, in which the amplitude of the motion is small compared with the diameter of the cylinder, it is to be expected that the force is dominated by the inertia of the accelerating fluid (Bearman et al., 1985).

This conclusion is tested further by considering the forces on a cylinder submerged in a tank of water with an initial elevation in the shape of a sine wave of wavelength twice the width of the tank, b. The wave elevation at the right-hand wall is plotted in Fig. 28 both for the wave only and for the wave over a cylinder submerged at the centre of the tank, depth $h/2$ below the mean water level. The wave motion is damped by the presence of the cylinder and in this case there is a slight increase in the oscillation frequency. The hydrostatic component is subtracted from the vertical force, and the time histories of horizontal and vertical hydrodynamic force coefficients are presented in Fig. 29. As the undisturbed sine wave is asymmetric and has maximum horizontal velocity and zero vertical velocity, we would expect the

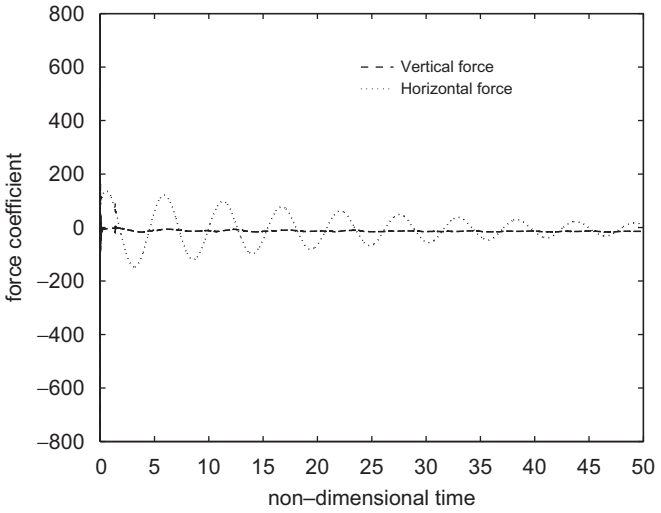

Fig. 29. Time history of forces on submerged cylinder under a half sine wave, Re = 200.

horizontal force on the cylinder to be maximum and the vertical force to be approximately zero. This is evident in Fig. 29, where the vertical force tends to approximately zero and the horizontal force oscillates with the same frequency and in phase with the wave motion recorded in Fig. 28. The horizontal force is dominated by inertia and oscillates with the horizontal fluid acceleration under the wave. When the wave peak is at the right-hand wall, the horizontal fluid acceleration at the cylinder is at its maximum, and when the wave trough is at the wall, the acceleration is at its minimum.

6. Conclusions

The adaptive quadtree volume of fluid method developed here shows great potential in the simulation of complex free surface flows. The new method uses CICSAM differencing for advection of the interface together with a PISO-type Navier–Stokes solution method for adapting quadtree grids. The adaptive quadtree results are in good agreement with analytical and other numerical data, and a sharp interface is maintained at the free surface. Results are calculated on adapting quadtree grids and equivalent uniform grids in which the panels are the same size as the smallest in the quadtree grid. In this way, it has been found that the same accuracy may be achieved using the adapting quadtree scheme as on the equivalent uniform grid and that a saving both in grid size and CPU is made.

The combination of dynamically adapting quadtree grids and Cartesian cut cells for a curved boundary is shown to be well suited to simulation of vortex shedding flow past a circular cylinder and results compare favourably with published data. The new method is applied to simulating linear and nonlinear viscous waves in a rectangular tank as well as viscous waves over a submerged cylinder. For the wave-only cases, the wave period is predicted well, but the amplitude is greater than that calculated analytically. The amplitude prediction improves in comparison with the linearised analytical solution for waves in less viscous fluid. For the wave over submerged cylinder cases, the cylinder is found to damp out and slightly alter the frequency of the wave motion. Hydrodynamic forces on the submerged cylinder under the wave are shown to be dominated by inertia.

The method could be extended to three dimensions using adaptive octree grids with Cartesian cut cells, although it would be very computationally expensive for practical cases. Measures to reduce the CPU time would have to be taken, such as use of multigrid iterations and possibly a domain decomposition approach, in which the Navier Stokes viscous model is combined with a fully nonlinear potential flow model.

Acknowledgements

The author is very grateful to the Royal Society for supporting this work through a Royal Society University Research Fellowship, 2000–2006.

References

Andrillon, Y., Alessandrini, B., 2004. A 2D + T VoF fully coupled formulation for the calculation of breaking free-surface flow. Journal of Marine Science Technology 8, 159–168.

Bearman, P.W., Downie, M.J., Graham, J.M.R., Obasaju, E.D., 1985. Forces on cylinders in viscous oscillatory flow at low Keulegan–Carpenter numbers. Journal of Fluid Mechanics 154, 337–356.

Causon, D.M., 1996. An efficient front tracking algorithm for multi-component fluid calculations with biomedical applications. Zeitscrift fur angewandte Mathematik und Mechanik 76 (S1), 371–372.

Dommermuth, D.G., Yue, D.K.P., 1987. Numerical simulations of non-linear axisymmetric flows with a free surface. Journal of Fluid Mechanics 178, 195–219.

Ferziger, J.H., Perić, M., 1996. Computational Methods for Fluid Dynamics. Springer, Berlin.

Greaves, D.M., 2004. Simulation of interface and free surface flows in a viscous fluid using adapting quadtree grids. International Journal for Numerical Methods in Fluids 44, 1093–1117.

Greaves, D.M., 2005. Simulation of viscous water column collapse using adapting hierarchical grids. International Journal for Numerical Methods in Fluids 50, 693–711.

Greaves, D.M., Borthwick, A.G.L., 1998. On the use of adaptive hierarchical meshes for numerical simulation of separated flows. International Journal for Numerical Methods in Fluids 26, 303–322.

Hirt, C.W., Nichols, B.D., 1981. Volume of Fluid (VoF) method for the dynamics of free boundaries. Journal of Computational Physics 39, 201–225.

Hyman, J.M., 1984. Numerical methods for tracking interfaces. Physica D 12, 396–407.

Issa, R.I., 1986. Solution of the implicitly discretised fluid flow equations by operator-splitting. Journal of Computational Physics 62 (1), 40–65.

Kleefsman, T.K.M., Veldman, A.E.P., 2004. An improved volume-of-fluid method for wave impact. In: Proceedings of ECCOMAS, Jyväskylä, 24–28 July 2004.

Lin, H., Atluri, S.N., 2001. The Meshless Local Petrov–Galerkin (MLPG) method for solving incompressible Navier–Stokes equations. Computer Modelling in Engineering and Sciences 2 (2), 117–142.

Losasso, F., Fedkiw, R., Osher, S., 2005. Spatially adaptive techniques for level set methods and incompressible flow. Computers and Fluids 35, 995–1010.

Ma, Q.W., Wu, G.X., Eatock Taylor, R., 2001a. Finite element simulation of fully nonlinear interaction between vertical cylinders and steep waves—part 1: methodology and numerical procedure. International Journal for Numerical Methods in Fluids 36, 265–285.

Ma, Q.W., Wu, G.X., Eatock Taylor, R., 2001b. Finite element simulation of fully nonlinear interaction between vertical cylinders and steep waves—part 2: numerical results and validation. International Journal for Numerical Methods in Fluids 36, 287–308.

Monaghan, J.J., 1994. Simulating free surface flows with SPH. Journal of Computational Physics 65, 179–214.

Qian, L., Causon, D.M., Ingram, D.M., Mingham, C.G., 2003. An efficient two-fluid solver for hydraulic flow problems. Journal of Hydraulic Engineering 129 (9), 688–696.

Qian, L., Causon, D.M., Mingham, C.G., Ingram, D.M., 2005. A free-surface capturing method for two fluid flows with moving bodies. Proceedings of Royal Society A 462 (2065), 21–42.

Sarpkaya, T., 1981. Mechanics of Wave Forces on Offshore Structures. Van Nostrand Reinhold Co., New York.

Tomiyama, A., Sou, A., Minagawa, H., Sakaguchi, T., 1993. Numerical analysis of a single bubble by VoF method. JSME International Journal, Series B 36, 51–56.

Tseng, Y.-H., Ferziger, J.H., 2003. A ghost-cell immersed boundary method for flow in complex geometry. Journal of Computational Physics 192, 593–623.

Ubbink, O., 1997. Numerical prediction of two fluid systems with sharp interfaces. Ph.D. Thesis, Imperial College of Science, Technology and Medicine, London.

Ubbink, O., Issa, R.L., 1999. A method for capturing sharp fluid interfaces on arbitrary meshes. Journal of Computational Physics 153, 26–50.

Wang, J.P., Borthwick, A.G.L., Eatock Taylor, R., 2004. Finite-volume type VOF method on dynamically adaptive quadtree grids. International Journal for Numerical Methods in Fluids 45, 485–508.

Wu, G.X., Eatock Taylor, R., Greaves, D.M., 2001. Viscous effect on the transient free surface flow in a two dimensional tank. Journal of Engineering Mathematics 40, 77–90.

Yang, G., Causon, D.M., Ingram, D.M., Saunders, R., Batten, P., 1997. A Cartesian cut cell method for compressible flows—part A: static body problems. The Aeronautical Journal, Paper 2119.

Yiu, K.F.C., Greaves, D.M., Cruz, S., Saalehi, A., Borthwick, A.G.L., 1995. Quadtree grid generation: information handling, boundary fitting and CFD applications. International Journal of Computers and Fluids 25 (8), 759–769.

Zhou, C.Y., Graham, J.M.R., 2000. A numerical study of cylinders in waves and currents. Journal of Fluids and Structures 14, 403–428.